JGR Oceans

RESEARCH ARTICLE
10.1029/2020JC017005

Wave-Enhanced Tracer Dispersion

Jim Thomas[1,2] **and Aman Gupta**[3]

[1]International Centre for Theoretical Sciences, Tata Institute of Fundamental Research, Bangalore, India, [2]Centre for Applicable Mathematics, Tata Institute of Fundamental Research, Bangalore, India, [3]Meteorological Institute, Ludwig-Maximilian University of Munich, Munich, Germany

Key Points:

- Oceanic datasets collected over the past decade indicate an increase in wave-to-balance energy ratio on moving from meso- to submesoscales
- We explore passive tracer dispersion by barotropic flows in quasi-geostrophic and wave dominant turbulent regimes using a reduced model
- Stirring and mixing of the passive tracer is enhanced in wave dominant regime when compared to quasi-geostrophic regime

Correspondence to:

J. Thomas,
jimthomas.edu@gmail.com

Citation:

Thomas, J., & Gupta, A. (2022). Wave-enhanced tracer dispersion. *Journal of Geophysical Research: Oceans*, *127*, e2020JC017005. https://doi.org/10.1029/2020JC017005

Received 22 NOV 2020
Accepted 23 JAN 2022

Abstract Recent oceanic datasets indicate high gravity wave-to-balance energy ratio at submesoscales. Idealized investigations exploring such wave-dominated regimes have found that waves can break up coherent vortices and generate energetic small scale flow structures, indicating that the turbulence phenomenology is very different in wave-dominated regimes when compared to the quasi-geostrophic regime. Motivated by these recent investigations revealing significant differences in the flow dynamics in quasi-geostrophic and wave-dominated regimes and multiple oceanic observations pointing out enhanced tracer stirring at submesoscales, in this paper we compare and contrast passive tracer dispersion by barotropic flows in quasi-geostrophic and wave-dominated turbulent regimes using the reduced model explored by Thomas and Yamada (2019), https://doi.org/10.1017/jfm.2019.465. On comparing passive tracer dispersion by barotropic flows in the two different regimes, we find that wave-dominated turbulent flows stir and mix tracer fields much more rapidly than quasi-geostrophic turbulent flows that consist of well-defined coherent vortices. The presence of energetic small-scale features in wave-dominated flows increases small-scale turbulent diffusivity and results in steeper tracer variance spectrum in wave-dominated flows compared to the quasi-geostrophic flows. Our findings point out that gravity waves can play an indirect role in enhancing tracer dispersion: waves modify the flow, generating energetic small-scale structures, that makes stirring of tracers more efficient. Despite our study being idealized, we speculate the qualitative phenomenology of waves indirectly enhancing tracer dispersion to be of significance at submesoscales in the world's oceans.

Plain Language Summary Recent oceanic datasets indicate high inertia-gravity wave energy levels at O (1–10) km submesoscales in the world's oceans. Inspired by these observations, we explore tracer dispersion by an idealized model that can access geostrophic turbulence regime, with large coherent vortices, and a wave-dominated regime, where high energy waves leads to the generation of energetic small-scale structures. On comparing tracer dispersion in the two regimes, we find that wave-dominated turbulent flows stir and mix tracer fields much more efficiently than geostrophic turbulent flows. Overall, wave-dominated flows facilitate faster transfer of tracer variance to small dissipative scales, resulting in steeper tracer variance spectra when compared to the tracer stirring in geostrophic turbulence regime. In the oceanographic community, inertia-gravity waves are often considered to be ineffective in stirring tracers. Our findings point out that inertia-gravity waves can play an indirect role in enhancing tracer dispersion. Waves can significantly modify the flow that stirs tracers, thereby indirectly enhancing the efficiency of tracer dispersion. Although our results were obtained using an idealized set up, we speculate that the qualitative phenomenological finding of waves indirectly enhancing tracer dispersion could be relevant at wave-dominated submesoscales in the world's oceans.

1. Introduction

Fluid flow in the ocean spans nine decades of spatial scales, from O (1,000 km) basin scales to O (mm) viscous Kolmogorov scales where the flow kinetic energy is dissipated. Although the earliest studies on oceanic fluid flow were primarily focused on the quasi-steady basin scale flow, closely followed by investigations aimed at understanding mesoscale ocean dynamics (Richardson, 2008; Warren & Wunsch, 1981; Wunsch & Ferrari, 2018), developments in the past few decades have been geared toward decoding submesoscale dynamics with horizontal scales of the order of 10 km and smaller (McWilliams, 2016). In this regard, a persistent feature seen in situ observations, satellite altimeter datasets, and state-of-the-art global scale ocean model outputs of the past decade is an increase in gravity wave-to-balance energy ratio as one moves from meso- to submesoscales. Submesoscales are seen to have much higher wave energy levels than mesoscales, with wave energy being one-to-two

orders of magnitude higher than balanced energy in multiple oceanographic regions (Bühler et al., 2014; Lien & Sanford, 2019; Qiu et al., 2017, 2018; Richman et al., 2012; Rocha et al., 2016; Savage et al., 2017; Tchilibou et al., 2018; Torres et al., 2018). Therefore on moving from meso- to submesoscales, one sees a transition from quasi-geostrophic turbulence dominated by the dynamics of the geostrophic balanced flow to a turbulence regime dominated by inertia-gravity waves.

Recent investigations, using two-dimensional and three-dimensional models (Thomas & Arun, 2020; Thomas & Daniel, 2020, 2021; Thomas & Yamada, 2019), aimed at developing a phenomenological understanding of a broad set of wave-dominated turbulent regimes indicate that the flow dynamics is significantly different in quasi-geostrophic turbulence and wave-dominated turbulence. Although specific details, such as the direction and magnitude of wave-balance energy transfers for example, depend on the kind of wave field (see table 2 in Thomas & Daniel, 2021), these studies point out that inertia-gravity waves can break up large-scale coherent vortices, thereby generating energetic small-scale structures. The two-dimensional models used by Thomas and Yamada (2019) and Thomas and Arun (2020) are models that are obtained by projecting the primitive equations onto the barotropic and a single baroclinic mode. In the absence of inertia-gravity waves these models reduce to two-mode quasi-geostrophic equations. In contrast, by retaining waves, these models access regimes that are inaccessible to balanced models generating quasi-geostrophic turbulence. Importantly, these reduced models capture the key features of generic wave-dominated turbulent regimes: waves breaking up coherent vortices and generating flows that have energetic small-scale structures.

In this paper, we compare and contrast between passive tracer dispersion by barotropic flows in quasi-geostrophic and wave-dominated turbulent regimes using the two-vertical-mode model used by Thomas and Yamada (2019), hereafter referred to as TY. Our work is inspired by oceanic observations that examine tracer stirring at submesoscales (Callies & Ferrari, 2013; Cole et al., 2010; Cole & Rudnick, 2012; Ferrari & Rudnick, 2000; Klymak et al., 2015; Kunze et al., 2015; Spiro Jaeger et al., 2020). These observations point toward a paradigm where submesoscale flows enhance tracer dispersion, with tracers being stirred much more efficiently than that one would anticipate based on quasi-geostrophic turbulence phenomenology. Given the broad set of physical processes that can generate submesoscale flows, the emerging datasets calls for dedicated process studies to examine how energetic submesoscales – generated by different mechanisms – will affect tracer dispersion. In this work we explore one such possibility using an idealized model: the presence of high energy inertia-gravity waves affecting tracer dispersion.

Since oceanic flows, and geophysical flows in general, are composed of multiple intertwined complex physical processes, several past works have tried isolating and studying the role of specific physical mechanisms that affect tracer dispersion and contribute toward turbulent diffusivity of flows. These include: using resonant wave interaction theory to compute the diffusivity generated by weakly nonlinear waves in the absence of the vortical mode (Benilov & Wolanski, 1992; Buhler & Holmes-Cerfon, 2009; Holmes-Cerfon et al., 2011; Sanderson & Okubo, 1988), numerically exploring tracer dispersion by the vortical mode in the absence of internal waves (Klein et al., 1998; Scott, 2006; Smith & Ferrari, 2009), numerical investigations of tracer dispersion by nonlinear breaking waves (Lelong & Sundermeyer, 2005; Lindzen, 1981; Randel & Garcia, 1994; M. A. Sundermeyer & Lelong, 2005), and the usage of analytically tractable Greens function approach to compute effective diffusivity of turbulent geophysical flows (Galperin & Sukoriansky, 2020; Sukoriansky et al., 2009). The present paper belongs to a similar category of idealized investigations, with the exception that we compare and contrast passive tracer dispersion by barotropic flows in wave-dominated regime with quasi-geostrophic regime using the reduced model of TY, thereby developing an understanding of how the key features of tracer dispersion differs in the two distinct regimes.

The plan for the paper is as follows: we describe the model and the set up in Section 2, forced-dissipative tracer experiments in Section 3, and freely evolving localized tracer experiments in Section 4, and summarize our study in Section 5.

2. Barotropic Flow Fields in QG and SW Regimes

The tracer dispersion study described in this paper is based on the model explored in detail by TY. In this section we provide a brief description of the model, the set up, and the main findings of the TY, before we examine tracer dispersion using the model.

The two-vertical-mode model used by TY is obtained by projecting the *f*-plane hydrostatic Boussinesq equations onto the barotropic and the first baroclinic mode. For example, the horizontal velocity field, $\boldsymbol{v}$, is expanded in vertical modes as: $\boldsymbol{v}(\boldsymbol{x}, z, t) = \boldsymbol{v}_T(\boldsymbol{x}, t) + \sqrt{2}\cos(\pi z/H)\boldsymbol{v}_C(\boldsymbol{x}, t)$, where $\boldsymbol{v}_T$ and $\boldsymbol{v}_C$ denote the barotropic and the first baroclinic horizontal velocity fields respectively, H is the depth of the ocean, and $\cos(\pi z/H)$ is the first baroclinic mode eigenfunction. Projecting the hydrostatic Boussinesq equations on the barotropic and first baroclinic mode, after eliminating buoyancy using hydrostatic balance, gives a reduced two-dimensional model. The equations so obtained were then non-dimensionalized, choosing the inertial timescale, $1/f$ (where f is the constant rotation rate) as the timescale and the horizontal length scale to be the deformation scale: NH/f. An arbitrary velocity scale U was used to non-dimensionalize velocity fields and the geostrophic balance condition using the velocity scale U was used to obtain the scale for baroclinic pressure (p_C). After non-dimensionalizing the reduced model, we obtain the equations:

$$\frac{\partial \zeta_T}{\partial t} + Ro\nabla \times (\boldsymbol{v}_T \cdot \nabla \boldsymbol{v}_T + \boldsymbol{v}_C \cdot \nabla \boldsymbol{v}_C + (\nabla \cdot \boldsymbol{v}_C)\boldsymbol{v}_C) = -\gamma \zeta_T - \nu \Delta^8 \zeta_T \tag{1a}$$

$$\frac{\partial \boldsymbol{v}_C}{\partial t} + \hat{\boldsymbol{z}} \times \boldsymbol{v}_C + \nabla p_C + Ro\,(\boldsymbol{v}_T \cdot \nabla \boldsymbol{v}_C + \boldsymbol{v}_C \cdot \nabla \boldsymbol{v}_T) = -\nu \Delta^8 \boldsymbol{v}_C \tag{1b}$$

$$\frac{\partial p_C}{\partial t} + \nabla \cdot \boldsymbol{v}_C + Ro\,(\boldsymbol{v}_T \cdot \nabla p_C) = -\nu \Delta^8 p_C \tag{1c}$$

In the variables above, subscripts T and C indicate barotropic and baroclinic fields respectively and $Ro = U/fL$ represents the Rossby number. The barotropic flow is divergence free and is entirely captured by the barotropic vorticity ζ_T, which is related to the barotropic streamfunction ψ_T via $\zeta_T = \nabla \times \boldsymbol{v}_T = \Delta \psi_T$. The baroclinic fields are on the other hand composed of both waves and balanced mode, denoted with subscripts W and G; for example, the baroclinic velocity field can be decomposed as $\boldsymbol{v}_C = \boldsymbol{v}_W + \boldsymbol{v}_G$. Therefore the two-vertical-mode model is composed of three components: T, G, and W. The schematics of the model and the three components are shown in Figure 1a. In the small Rossby number regime, $Ro \ll 1$, removing waves from the model leads to the two-mode quasi-geostrophic equations (see equations 2.18 in TY), that captures interactions between the barotropic (T) and baroclinic balanced mode (G). In such quasi-geostrophic turbulent regimes, the baroclinic balanced mode transfers energy to the barotropic flow, as indicated by the blue arrow in Figure 1a.

The work described in TY was inspired by observations of regions of high gravity wave energy levels in the world's oceans. In situ, satellite altimeter, and global scale ocean model outputs indicate that the balanced energy levels could be one-to-two orders of magnitude lower than wave energy levels in certain regions (Bühler et al., 2014; Lien & Sanford, 2019; Qiu et al., 2017; Qiu et al., 2018; Richman et al., 2012; Savage et al., 2017; Tchilibou et al., 2018; Torres et al., 2018). Notably, low baroclinic mode internal tides were seen to be the dominant wave field in some of the high wave energy regions, such as the north of Hawaii, North Pacific, and North Equatorial Current regions, for example. Consequently, TY explored interactions and the energy exchanges between the first baroclinic mode gravity waves and balanced flows and found significant energy exchanges in a regime identified as "Strong Wave" (SW) regime, with the scaling $E_T/E_W \sim Ro^2$, where E_T and E_W denote barotropic and wave energies respectively. The red arrows in Figure 1a indicates the new energy transfers that appear due to waves, in addition to the blue arrow indicating geostrophic energy transfer. Therefore, in the SW regime, the quasi-geostrophic energy transfer is a subset of all the energy transfers that appear in the two-vertical-mode model. Energy transfers via gravity waves form a significant contribution toward the overall energetics of the two-vertical-mode model.

To set up the SW regime, as in TY, we initialized the barotropic and the baroclinic modes at low wavenumbers, $k < 6$, with white noise such that the initial energy was $E_T = E_G \sim Ro^2$ and $E_W \sim 1$ (we used $Ro = 0.1$ throughout). The QG regime is then a subset of the SW regime, where the waves were not initialized. We then integrated Equation 1 using dealiased pseudospectral numerical scheme. A doubly periodic domain, $(x, y) \in [0,2\pi]^2$, with 384^2 grid points was used, yielding maximum wavenumber $k_{\max} = 128$ after dealiasing. Figure 1b shows the energy spectrum of waves and the barotropic flow after the initial transients died off. Observe that the wave spectrum dominates over the barotropic spectrum for $k \leq 10$, this being the signature of the SW regime. At the low wavenumbers, the wave field is purely linear: Figure 1c shows the frequency spectrum of the wave field for three different wavenumbers. Notice how the frequency spectrum peaks at values predicted by the inertia-gravity waves' dispersion relationship: $\omega(k) = \sqrt{1 + k^2}$ (denoted by dashed black vertical lines in the figure), and decays away from it. As detailed in TY, the energy transfers from waves to the balanced flow take place almost

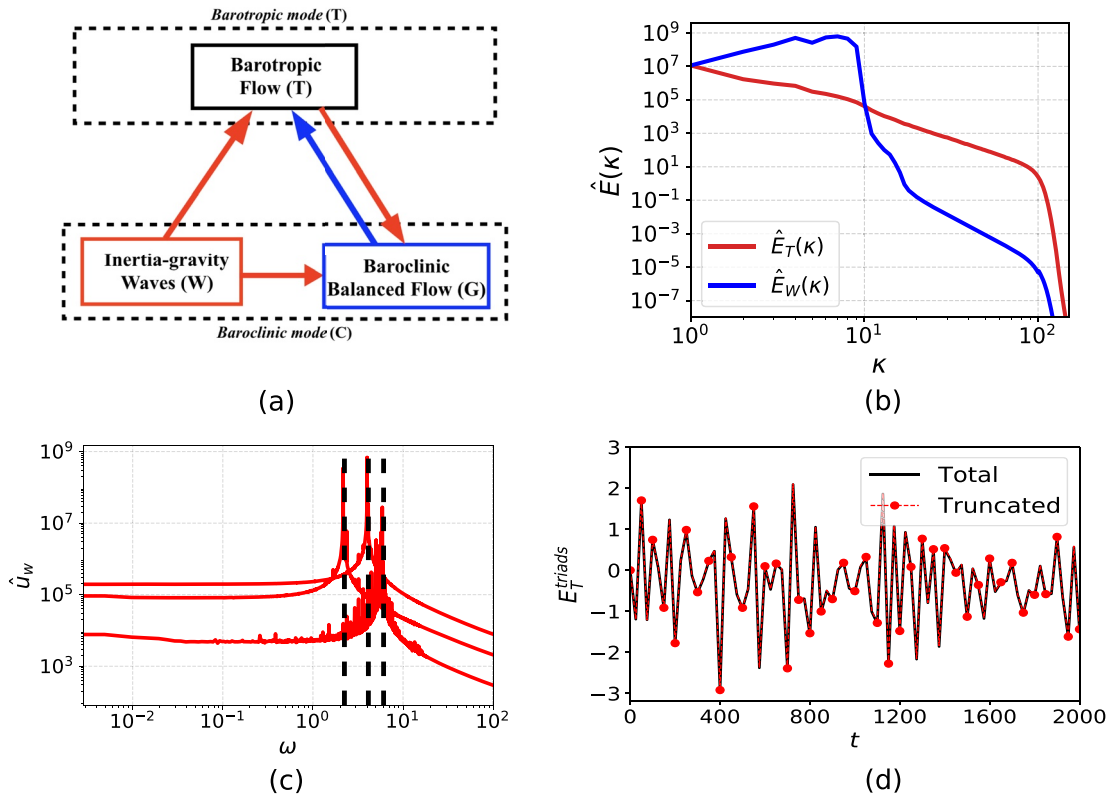

Figure 1. (a) Energy flow pathways for the model given in Equation 1. Blue arrow shows the energy transfer in the absence of waves, this being the sole energy transfer in QG turbulence. The red arrows indicate the additional energy transfers that appear in the SW regime. (b) Energy spectrum of wave (blue) and barotropic flow (red) in the SW regime. (c) Frequency spectrum of waves for wavenumbers $k = 2$, 4, and 6. The dashed black lines denote frequencies based on the dispersion relationship $\omega(k) = \sqrt{1 + k^2}$. (d) Black curve indicates the energy transfer to the barotropic flow, E_T^{triads}, while the red curve indicates E_T^{triads} computed by truncating all the fields to $k \leq 10$. Both curves have been normalized by their root-mean-square average in the time window $t = 0$–2,000.

exclusively at scales where wave spectrum lies over the balanced spectrum, that is, at scales $k \leq 10$ in Figure 1b. To see this explicitly, we have to look at the energy equation. For the barotropic mode, multiplying Equation 1a with ψ_T and integrating over the domain gives us the barotropic energy equation:

$$E_T(t) - E_T(0) = E_T^{\text{triads}} - \mathcal{E}_T - D_T \tag{2}$$

Above equation indicates that the changes in the barotropic energy (left hand side) is due to triadic interactions between the modes (E_T^{triads}), small-scale dissipation ($\mathcal{E}_T$), and large-scale drag (D_T). The black curve in Figure 1d shows the triadic energy transfer term E_T^{triads} normalized by its root-mean-square value computed during the time interval $t = 0$–2,000. Additionally, we truncated all the physical fields to $k \leq 10$, retaining only the large-scale structure, and then computed the transfer term E_T^{triads}. For wave fields that exhibit a forward energy flux, with energy being continuously transferred to small scales, such a transfer term computed using fields restricted to low wavenumbers will deviate from the total transfer term as time progresses. The red curve in Figure 1d shows the truncated transfer term normalized by its root-mean-square value, which is almost identical to the total transfer term. Therefore, all the energy transfers to the barotropic flow takes place at low wavenumbers, where wave energy exceeds barotropic energy. With the setup we have, there is no forward flux of wave energy, which is why TY explored the regimes without having to externally force the physical fields. For a comprehensive description of all the energy transfers and comparison with truncated fields, we refer the reader to figure 8 in TY.

Snapshots of the barotropic vorticity field for the QG and the SW cases are shown in Figures 2a and 2b. Observe that the QG case is composed of well-formed coherent vortices – some large and some small vortices. In contrast, the SW flow is composed of energetic small-scale structures distributed throughout the domain. Although there is a tendency to form large coherent vortices via vortex mergers, high energy waves interact with the vortices and keeps generating energetic small-scale features. The barotropic energy spectra of these two flows are shown in

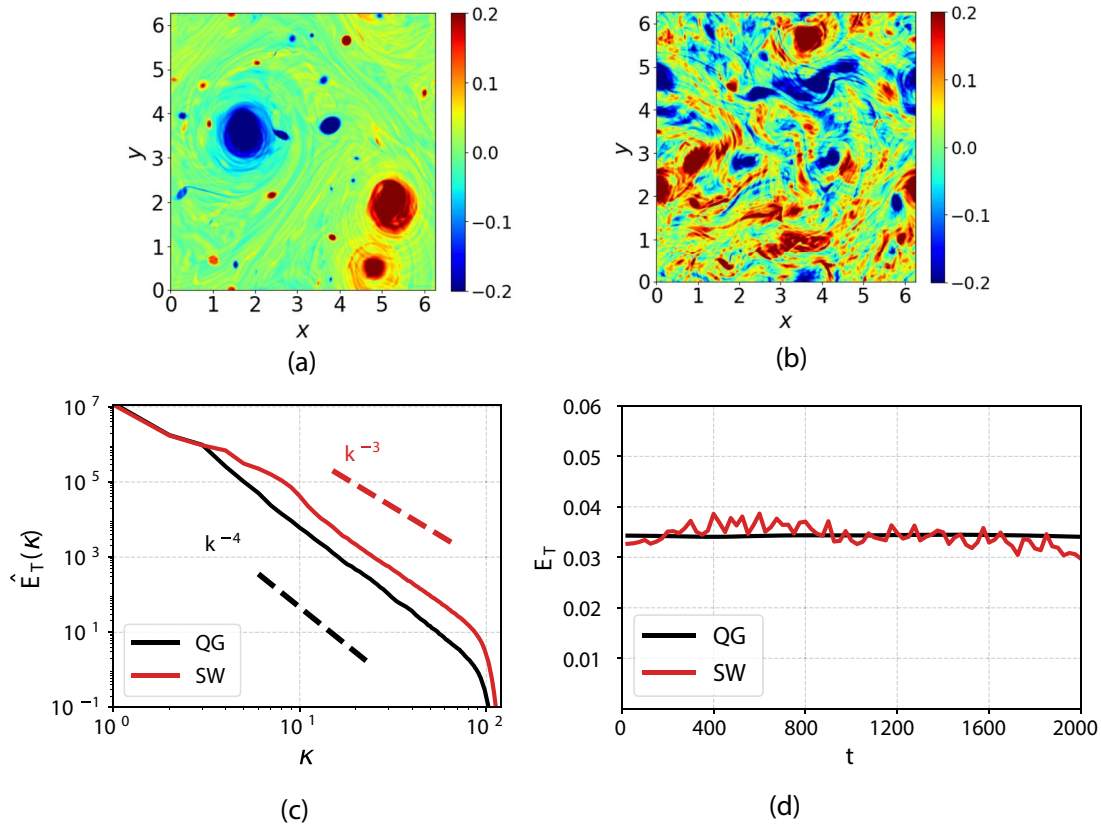

Figure 2. Top row shows barotropic vorticity field in (a) QG and (b) SW regime at $t = 1{,}200$. Panel (c) shows the energy spectra of the barotropic flow in QG and SW cases obtained by time averaging from $t = 800$ to $t = 1{,}600$. Straight lines with slopes −3 and −4 are added for reference. Panel (d) shows the barotropic energy time series for QG and SW cases.

Figure 2c. Notice that the energy spectrum of the SW flow shows more energy at higher wavenumbers (or smaller scales) than the QG flow, this being a consequence of the small scales generated by wave-balance interactions.

Due to significant energy transfer from waves to the barotropic flow, the barotropic energy increases with time (see figure 5 in TY). We added the drag term $-\gamma\zeta_T$ in the barotropic Equation 1a to equilibrate the barotropic flow, so as to generate barotropic flows with same energy levels for QG and SW cases, as can be seen in Figure 2d. The presence of linear drag ensured that the barotropic energy did not increase with time in our present work. The addition of the linear drag term in the barotropic Equation 1a is the only change between the flow equations used in this work to generate QG and SW flows compared to that of TY. No drag term was used in TY, whereas we used a drag term to get the barotropic energy levels to saturate to the same magnitude in both QG and SW regimes.

Summarizing the discussion so far, we note that the presence of inertia-gravity waves can severely modify the balanced flow dynamics. While waves play no role in the QG regime dominated by large-scale coherent vortices, SW is a regime where inertia-gravity waves interact with the balanced flow and generates energetic small-scale structures. The SW regime specifically is expected to capture dynamics of oceanic regions where low baroclinic mode internal tidal energy is high. Given that this simple and easily tractable model allows access to two-different dynamic regimes – QG and SW – and the recent findings of wave dominating regions in the world's oceans, in this work we will explore how the characteristic features of tracer dispersion differ in the two different dynamic regimes.

We conclude this section by pointing out that the transition in flow dynamics, that is, the features of the barotropic flow changing from QG to SW regime as seen in the top row of Figure 2, was consistently observed in the three-dimensional studies of Thomas and Daniel (2020) and Thomas and Daniel (2021). The non-divergent barotropic flow therefore forms the simplest two-dimensional flow that transitions in its dynamic features based on the wave energy level. We therefore treat the barotropic flow as a "prototype flow" that captures the essence of the transition between QG and SW regimes and explore the changes a passive tracer field stirred by the barotropic

flow experiences in the two different regimes. While the idealization we take advantage of would definitely result in loss of specific details seen in tracer dispersion experiments in more complex set ups, the qualitative phenomenological understanding we gain is expected to carry over beyond the simplifications we make. We refer the reader to Appendix A for insights on exploring tracer dispersion using the full two-vertical-mode model (instead of the barotropic flow alone) and shallow water models.

3. Forced-Dissipative Tracer Experiments

In this section we will investigate how a passive tracer field maintained by forcing at large scales and dissipated at small scales will be influenced by the barotropic flows in QG and SW regimes. The tracer evolution equation is

$$\frac{\partial \theta}{\partial t} + \boldsymbol{v} \cdot \nabla \theta = f_\theta - \alpha \Delta^8 \theta \tag{3}$$

where θ is the passive tracer advected by the barotropic flow $\boldsymbol{v}$ (hereafter we will omit the subscript "T" for the barotropic flow, which was used in Equation 1), f_θ is a stochastic forcing term injecting tracer variance at large scales and $\alpha\Delta^8\theta$ is the hyperdissipation term dissipating tracer variance at grid scale.

We numerically integrated Equation 3 in QG and SW regimes with same barotropic energy levels, seen in Figure 2d. We used the stochastic forcing scheme discussed in Alvelius (1999) to ensure a constant rate of tracer variance injection, forcing tracer variance at low wavenumbers, $5 \leq k \leq 6$, as white noise and chose $\alpha = 10^{-34}$ in Equation 3, thereby confining tracer variance dissipation to $k \sim 100$. This set up provided a broad set of inviscid scales for the tracer field, allowing the tracer field to be stirred and filamented by the flow, tracer variance gradually cascading to smaller and smaller scales, eventually reaching grid scales and being dissipated.

We observed that the barotropic flow fields were fully developed by $t \sim 200$ in Figure 2d and started advecting the tracer field by the flow at $t = 600$. After initial transients, both tracer fields equilibrated at a statistical steady state around $t = 700$. We therefore performed all the tracer diagnosis from $t = 800$–$1{,}600$, this being the time interval during which time averaging of various statistical quantities described below were performed. During this time interval, we observed that $\overline{E_T}^{QG} / \overline{E_T}^{SW} = 1.000\,5$ (where over bar denotes time averaging), indicating that both QG and SW barotropic flows had almost identical mean energy levels.

Snapshots of the tracer fields advected by the QG and SW flows are shown in Figures 3a and 3b, while corresponding plots showing spatial structure of tracer gradient are given in Figures 3c and 3d. In the QG case, where the flow is dominated by well-defined coherent vortices, most of the tracer stirring takes place in straining regions between vortices. This feature can be seen in Figures 3a and 3c – observe that the tracer and its gradient attain intermittently large values in straining regions between vortices, these being regions where stirring by the eddies are strong. In contrast, away from high straining regions, especially inside coherent vortices, the tracer field and its gradient are homogenized and take up low values. Coherent vortices are in general known to be transport barriers with negligible effective diffusivity inside them (see e.g., discussions in Shuckburgh & Haynes, 2003). In contrast, stirring and mixing of the tracer is much broadly distributed in the SW case, as seen in Figures 3b and 3d. The spatial intermittency in regions where efficient stirring of the tracer take place is a key difference between QG and SW flows. Stirring by the QG flow is much more spatially localized and intermittent when compared to stirring by the SW flow, which is broadly spread over the domain.

The spatial intermittency in stirring by QG and SW flows can be seen in the histograms of tracer field and the tracer gradient fields shown in Figures 4a and 4b. In Figure 4a showing the histogram of the tracer field, we added a Gaussian curve which is indicated by the dashed blue curve. Notice that the tracer fields in both QG and SW flows depart from the Gaussian, although the QG case is relatively more fat-tailed than the SW flow. The kurtosis for the QG flow is 7.4, while that of SW flow is 6.1. In addition to the higher kurtosis, some level of asymmetry (especially for density values below 10^{-2}) and therefore skewness is seen in Figure 4a for histogram of the tracer field. However, the magnitude of the skewness is quite small and the sign of skewness was seen to change unpredictably for different tracer experiments we examined. Different experimental realizations were seen to have fluctuating (positive or negative) small skewness values. In contrast, the higher kurtosis for the QG case when compared to the SW case was a persistent feature that was observed in all realizations of tracer fields we examined in QG and SW flows.

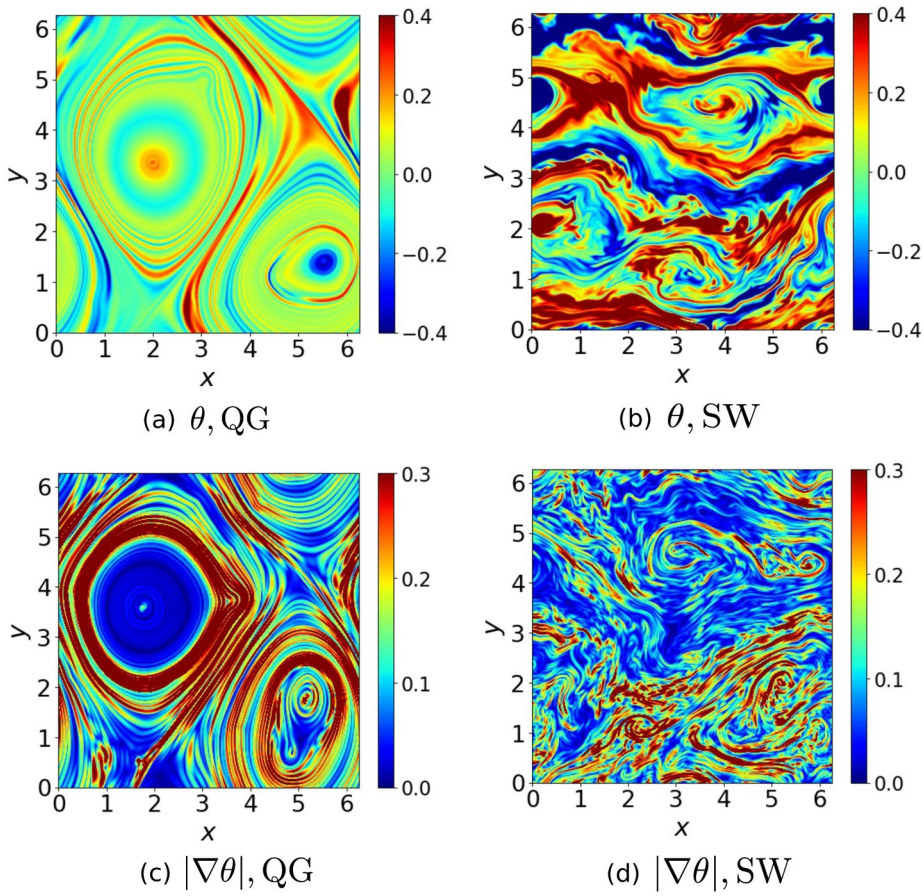

Figure 3. Panels (a) and (b) show snapshots of the spatial structure of the tracer field while panels (c) and (d) show the spatial structure of the gradient of the tracer field, all at $t = 1{,}200$. Observe that the tracer field and its gradient are localized and spatially intermittent in the QG case shown in (a) and (c), while the fields are broadly spread and less intermittent in (b) and (d) for the SW flow.

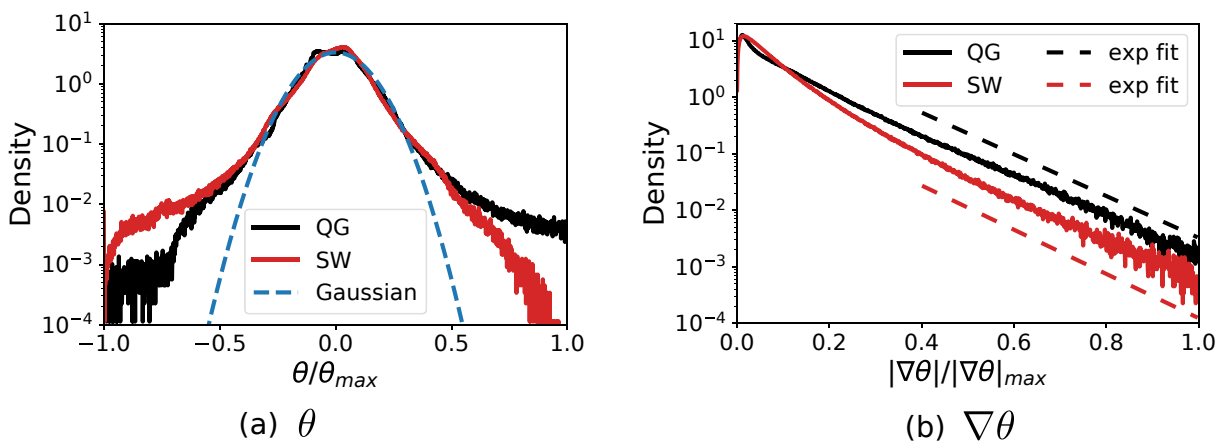

Figure 4. Panel (a) shows the histogram of the tracer field normalized by the maximum value of the tracer field. The kurtosis of the histograms are: $K_{QG} = 7.4$ and $K_{SW} = 6.1$. The blue dashed curve is a Gaussian curve for comparison. Panel (b) shows the histogram of the tracer gradient normalized by tracer gradient maximum for QG and SW flows. The dashed lines are exponential curves to indicate that the tails of the tracer gradient histograms decay exponentially. The fourth moments of the tracer gradient are: $M_{QG} = 3.4 \times 10^{-3}$ and $M_{SW} = 1.5 \times 10^{-3}$.

The contrast in kurtosis is more explicitly seen in Figure 4b showing the histogram of the gradient of the tracer field. The dashed lines are exponential curves (which appear as straight lines due to the log scale used for plotting), added to the figure to indicate that at extreme values the histograms have an exponential nature. Similar to the tracer field's histogram, the tracer gradient histogram also shows higher level of fat-tailedness for the QG case compared to the SW case. The fourth moments of the histogram are 3.4×10^{-3} for the QG case and 1.5×10^{-3} for the SW case. The higher value for the moments for the QG case in comparison to the SW case reflects the higher spatial intermittency of the tracer field and its gradient in the QG case in comparison to the SW case, as seen in physical fields shown in Figure 3.

Our diagnosis reveal that the SW flow is more efficient in stirring and mixing tracer fields when compared to the QG flow. The richer and energetic small-scale features in the SW flow generates filaments of tracer field all over the domain, as opposed to the spatially intermittent stirring that is efficient in specific regions of the domain in the QG case. To get a better handle on the transfer of tracer variance from large domain scales to small dissipative scales, we will now examine the flux of tracer variance. To construct the tracer variance flux equation, we define $\tilde{\theta}_L$ as the tracer field restricted to scales greater than or equal to a cut-off scale L. $\tilde{\theta}_L$ is therefore obtained by a spectral filter that removes all components of the tracer field θ that is smaller than the cut off scale L or wavenumbers higher than $k_L = 2\pi/L$, that is, $\tilde{\theta}_L = \mathcal{F}^{-1}\left(\hat{\theta}(k \leq k_L)\right)$ where $\hat{\theta}$ is the Fourier transform of θ, and $\mathcal{F}^{-1}$ denotes the inverse Fourier transform. We apply the spectral filter to the tracer Equation 3 to get

$$\frac{\partial \tilde{\theta}_L}{\partial t} + \widetilde{(\boldsymbol{v} \cdot \nabla \theta)}_L = \tilde{f}_L - \alpha \Delta^8 \tilde{\theta}_L \tag{4}$$

We multiply above equation by $\tilde{\theta}_L$ and manipulate the resulting equation to obtain:

$$\frac{\partial}{\partial t}\left(\frac{\tilde{\theta}_L^2}{2}\right) + \nabla \cdot \left(\tilde{\theta}_L \widetilde{(\theta \boldsymbol{v})}_L\right) = \underbrace{\left(\widetilde{(\theta \boldsymbol{v})}_L \cdot \nabla \tilde{\theta}\right)}_{-\tilde{\Pi}_L} + \tilde{F}_L - \tilde{D}_L \tag{5}$$

Above equation governs the time evolution of $(1/2)\tilde{\theta}_L^2$, that is, tracer variance associated with scales larger than and equal to L (see chapter 13 of Pope, 2000 for derivation of similar equations via filtering). The term $\widetilde{(\theta \boldsymbol{v})}_L$ denotes the field obtained by filtering the product of tracer and the velocity field. $\tilde{F}_L$ and $\tilde{D}_L$ denote filtered tracer variance injection and tracer variance dissipation. The second term on the left hand side of Equation 5 is responsible for transport of the large-scale tracer field in the domain. On integrating the above equation over the domain, this divergence term makes no net contribution. The first term on the right hand side of Equation 5, $\tilde{\Pi}_L = -\left(\widetilde{(\theta \boldsymbol{v})}_L \cdot \nabla \tilde{\theta}\right)$, does not vanish on integrating over the domain. $\tilde{\Pi}_L$ is the tracer variance flux and is responsible for the transfer of tracer variance from scales larger than or equal to L to smaller scales.

Figures 5a and 5b show $\tilde{\Pi}_L$ for the QG and SW cases normalized by their respective root-means-square values for $k_L = 30$. Similar spatial plots of fluxes are shown in Figures 5d and 5e for $k_L = 70$. The spatial plots of the fluxes were computed and time-averaged to obtain these figures. Observe that fluxes have both positive and negative values over the domain. Although $\tilde{\Pi}_L$ integrated over the whole domain – which gives the net flux of tracer variance to scales smaller than L – is positive, locally $\tilde{\Pi}_L$ can have negative values. Compare Figures 5a and 5b. Observe that the SW case has high values of $\tilde{\Pi}_L$ distributed over larger areas of the domain than the QG case. A similar conclusion is reached by comparing Figures 5d and 5e – the tracer field for the SW flow has larger regions of downscale tracer variance flux. These inferences are quantified by histograms of fluxes shown in Figures 5c and 5f. The mean of the histograms are shown by dashed vertical lines. Although the means are positive for both cases, indicating a net downscale transfer of tracer variance, the mean for the SW case is five to six times higher than the QG case. Our conclusions based on examining the spatial structure of fluxes is concomitant with the previous inferences of efficient stirring of the tracer field in broader regions of the domain for the SW flow when compared to the QG flow. Tracer variance flux takes higher values over much larger parts of the domain in the SW case when compared to the QG case, resulting in enhanced stirring and transfer of tracer variance from large forcing scales to small dissipative scales.

To compare the efficiency of stirring at different scales, we will now examine norms of the tracer field (Thiffeault, 2012). The q-norm of θ is defined as:

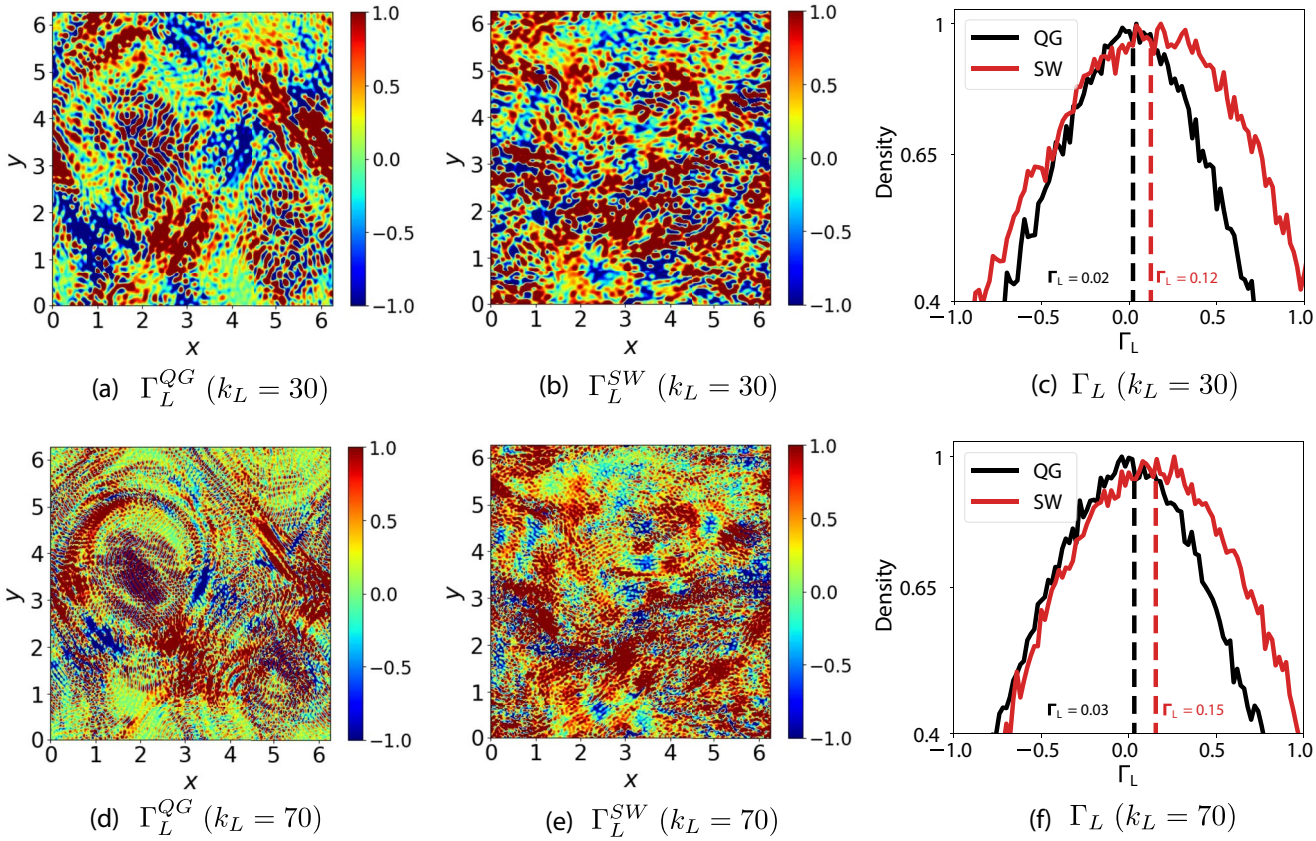

Figure 5. Top row shows spatial structure of normalized tracer variance flux, $\Gamma_L = \tilde{\Pi}_L/\tilde{\Pi}_L^{\mathrm{RMS}}$, for (a) QG (b) SW for $k_L = 30$. The histogram of fluxes are shown in panel (c). Bottom row shows same quantities as the top row for $k_L = 70$.

$$||\theta||_q = \sum_{k\neq 0} \left(k^{2q}|\hat{\theta}_k|^2\right)^{1/2} \tag{6}$$

As seen above, q-norm is obtained by taking appropriate moments of the tracer field in spectral space and summing over all wavenumbers. For $q = 0$, the expression in Equation 6 is proportional to the square root of tracer variance while for $q = 1$, Equation 6 is proportional to tracer gradient integrated over the domain. Furthermore, q in the q-norm above can take negative values. For example, $q = -1$ and $q = -2$ are integrated estimates for $(-\Delta)^{-1/2}\theta$ and $-\Delta\theta$.

The q-norm is essentially a metric that provides us a weighted estimate of the tracer field with respect to spatial scales. By choosing $q > 1$, we get an estimate for the tracer field at higher wavenumbers or smaller scales. On the other hand, $q < 0$ gives us tracer field estimate at small wavenumbers or large scales. As detailed in Thiffeault (2012), the q-norm is useful in estimating scale-dependent efficiency of stirring of tracers by different flows. Efficiency of stirring based on q-norms for comparing QG and SW flows can be defined as:

$$\eta = ||\theta^{\mathrm{QG}}||_q/||\theta^{\mathrm{SW}}||_q \tag{7}$$

The efficiency η, constructed as the ratio of QG and SW q-norms gives an estimate for the relative tracer fluctuations at different scales. Suppose for $q > 0$ we obtained $\eta < 1$. This implies that the q-norm for SW flow is higher than that for QG flow, indicating relatively lower tracer fluctuations at high wavenumbers for the QG case and thereby implies better stirring in the QG case (since lower tracer fluctuations at a certain scale means that there is stronger stirring, expelling the tracer field to smaller scales at a faster rate). On the contrary, if we obtained $\eta > 1$ for $q > 0$, that would indicate that the SW flow is more efficient in stirring at small scales, since the q-norm for the SW case is less than that of the QG case.

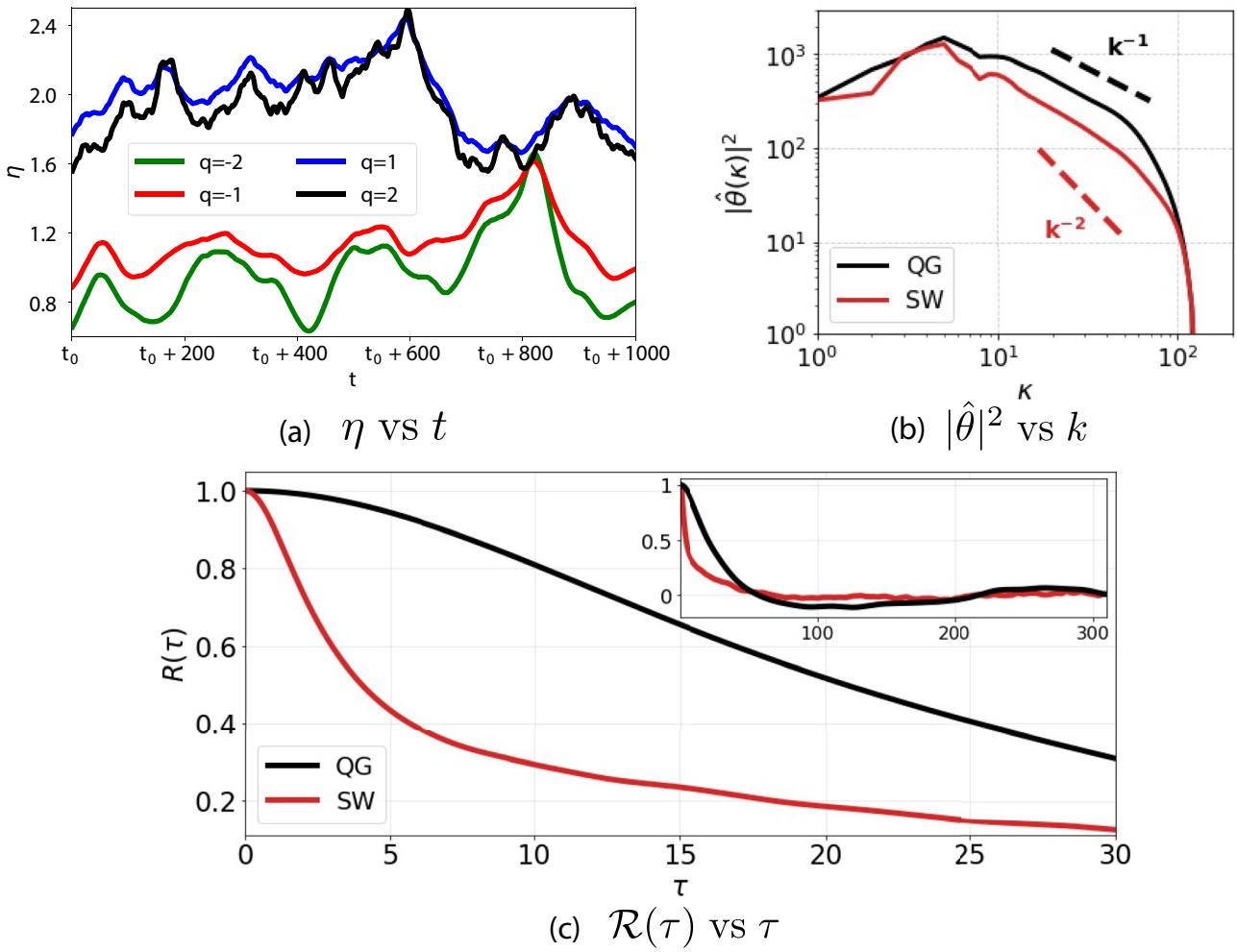

Figure 6. (a) Time series of efficiency, η, for different q. $t_0 = 600$ above. (b) Tracer variance spectra for QG and SW flows. Straight lines with slope -1 and -2 are added for reference. (c) Time series of autocorrelation, $\mathcal{R}(\tau)$. Main figure shows a short period while the inset shows a longer duration.

To examine stirring efficiency at different scales we computed η in Equation 7 for $q = -2, -1, 1$, and 2 and the time series of the efficiencies are given in Figure 6a. We observe that η is close to 1 for $q = -2$ and -1. This means that at large scales the stirring capabilities of the QG and SW flows are more or less comparable. On the other hand, as seen in Figure 6a, η is close to 2 for $q = 1$ and 2. Therefore, at smaller scales the SW flow is twice as efficient as the QG flow in stirring the tracer field. Our estimation of stirring efficiencies for different q directly reveals the scale-dependent stirring tendencies of the two flows. Although stirring tendencies are comparable for the two flows at large scales, the SW flow is more efficient than QG flow at smaller scales. The notable differences in the stirring capabilities of the tracer field across scales in QG and SW cases leads to significant differences in the tracer variance spectrum in the two regimes, as seen in Figure 6b showing the tracer variance spectra for the two cases. The enhanced small-scale stirring by the SW flow leads to much more depletion of tracer variance at small scales in the SW regime, as seen in Figure 6b, resulting in a steeper tracer variance spectrum in the SW case relative to the QG case.

To complete our analysis of forced-dissipative tracer experiments, we will now examine the mixing timescale of the tracers in the two regimes. For this, we define the autocorrelation of the tracer field as:

$$\mathcal{R}(\tau) = \{\theta(t)\theta(t+\tau)\} \tag{8}$$

where curly braces above indicate ensemble averaging. $\mathcal{R}$ measures the correlation of the tracer field with itself and gives an estimate of the "memory" of the tracer field. A tracer field that is getting mixed on a fast timescale

will have $\mathcal{R}$ decay from 1 at $\tau = 0$ to low values in a relatively short duration. On the other hand, a slowly mixing tracer field will have $\mathcal{R}$ decrease on a much longer timescale. The rate at which $\mathcal{R}$ decay is therefore a measure of how fast a tracer field mixes (see discussions in Qi & Majda, 2018 and Majda & Kramer, 1999). We computed $\mathcal{R}$ using tracer time series collected from 10,000 grid points in the domain and Figure 6c shows the evolution of $\mathcal{R}$ for the two flows. Observe that $\mathcal{R}$ drops much faster for the SW flow compared to the QG flow. Time integrating $\mathcal{R}$ would provide us with a timescale for mixing. We define two mixing timescales, similar to that employed by Qi and Majda (2018):

$$\tau_{\text{mix}}^{\text{abs}} = \int_0^\infty |\mathcal{R}(\tau)| d\tau \quad \text{and} \quad \tau_{\text{mix}} = \left| \int_0^\infty \mathcal{R}(\tau) d\tau \right| \tag{9}$$

On calculating the mixing timescales above, we obtained $\tau_{\text{mix}}^{\text{abs}}(\text{QG})/\tau_{\text{mix}}^{\text{abs}}(\text{SW}) = 2.75$ and $\tau_{\text{mix}}(\text{QG})/\tau_{\text{mix}}(\text{SW}) = 2.09$. The mixing timescale for the SW flow is therefore less than half the mixing timescale of the QG flow, implying that the SW flow is overall more efficient than the QG flow in mixing tracers.

4. Freely Evolving Tracer Experiments

In the previous section we explored the dynamics of a passive tracer that was forced at large scales and dissipated at small scales, thereby maintaining an equilibrated tracer field over the entire domain. The forced-dissipative experiments and our diagnosis revealed that stirring in the SW regime is enhanced at smaller scales, when compared with the QG case. In this section we will explore how spatially localized blobs of tracers evolve in the two regimes, and get a handle on the turbulent diffusivity of the flows. The localized-in-space initial value tracer experiments described in this section are inspired by oceanographic field campaigns that release dye tracers in different locations in the ocean and track the tracer's subsequent evolution to estimate turbulent diffusivity of the flow (Ledwell et al., 1993; Polzin & Ferrari, 2004; Shcherbina et al., 2015; M. Sundermeyer & Ledwell, 2001; M. A. Sundermeyer et al., 2019).

For the freely evolving localized tracer stirring experiments, we initialized Gaussian blobs of tracer $\theta(x, y, t = 0) = \exp\left(-\left((x - x_0)^2 + (y - y_0)^2\right)/a^2\right)$ and chose $a = 2\pi/80$ so that the initial blobs were 1/80th the size of the domain. We used 30 different ensembles for both QG and SW flows, by choosing different values for (x_0, y_0), ensuring that the initial tracer locations spanned over the entire domain. We advected the tracer field by the same flows shown in Figure 2, as in the previous section, but this time integrating Equation 3 with $f_\theta = 0$, that is, no tracer forcing. Tracer blobs were initialized at $t = 1{,}200$ and were advected up to $t = 1{,}400$. Beyond this time limit, the small-scale parts of the tracer fields were seen to get severely ruptured and dissipated at grid scale. Since the time interval for integration was seen to be sufficient for the large-scale tracer patches to reach domain scale, due to the tracer blobs being stretched and deformed by the flow, we chose $\Delta t = 200$ as the length of our time interval.

Out of the 30 ensemble members, three examples for QG and SW flows are given in the top row of Figure 7. Overall we found that the SW flow stirred the tracer blobs into longer convoluted patterns than the QG flow, as can be seen by comparing Figures 7a and 7b. Multiplying the tracer Equation 3 (without the forcing term f_θ) with θ and integrating over the domain we get the tracer variance equation:

$$\frac{d}{dt} < \theta^2 >= -D_\theta \tag{10}$$

where angle brackets indicate integration over the entire domain and D_θ is the dissipation of tracer variance at small scales. Contrary to the forced-dissipative experiments considered in the previous section, where tracer variance reaches an equilibrated state, the freely evolving experiments are characterized by tracer variance decaying with time. Although the advective terms do not appear explicitly in Equation 10, their action of generating finer scales in the tracer field accelerates transfer of the tracer variance to dissipative scales. Figure 7c shows the time series of ensemble averaged tracer variance for QG and SW flows. The more efficient stirring of the tracer blobs by the SW flow than the QG flow results in higher drop of tracer variance in the SW flow: observe that about 21% of tracer variance is lost in QG flow while 48% is the tracer variance loss in the SW flow. From Equation 10, balancing rate of change of tracer variance with dissipation gives us a mixing timescale, T_{mix}, representative of the timescale required for the transfer of tracer variance toward dissipative scales as:

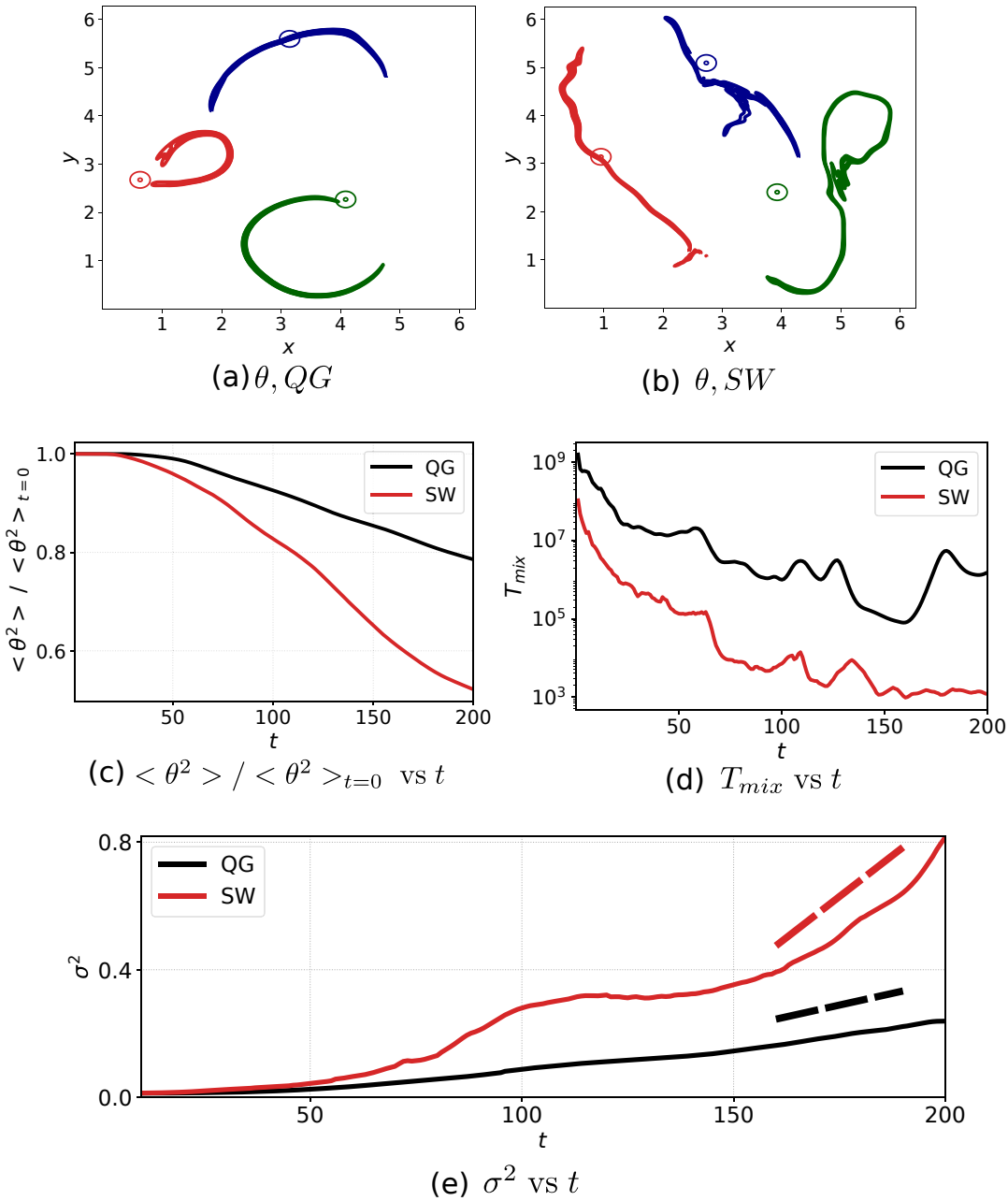

Figure 7. Top row shows tracer initial state (Gaussian blobs indicated as concentric circles) and final stretched states for (a) QG and (b) SW regimes for three ensemble members. Second row shows time series of (c) ensemble averaged tracer variance normalized by initial variance and (d) ensemble averaged T_{mix}. Panel (e) shows time series of ensemble averaged σ^2. Based on a linear fit for σ^2 versus t, we found the ratio of effective diffusivity of SW and QG flow to be $(\mathcal{K}_{SW}/\mathcal{K}_{QG})_{t=150-200} = 4.42$.

$$T_{\text{mix}}(t) = -\frac{< \theta^2 >}{D_\theta} \tag{11}$$

Figure 7d shows T_{mix} for QG and SW cases. Observe that T_{mix} for the QG flow is two orders or more higher than for the SW flow. The enhanced stirring and mixing properties of the SW flow leads to lower mixing time in the SW case than in the QG case.

We will now estimate the diffusivities of the QG and SW flows based on the time evolution of the tracer blobs (Csanady, 1980; Fischer et al., 1979; Peeters et al., 1996; Taylor, 1922). For the diffusivity estimation, we first computed the center of mass (x_{CM}, y_{CM}) of the tracer blobs as

$$(x_{CM}, y_{CM}) = \iint (x, y)\theta \; dxdy \Big/ \iint \theta \; dxdy \tag{12}$$

which was used to compute the variances as

$$\sigma_{xx} = \iint (x - x_{CM})^2\theta \; dxdy \Big/ \iint \theta \; dxdy \tag{13a}$$

$$\sigma_{xy} = \sigma_{yx} = \iint (x - x_{CM})(y - y_{CM})\theta \; dxdy \Big/ \iint \theta \; dxdy \tag{13b}$$

$$\sigma_{yy} = \iint (y - y_{CM})^2\theta \; dxdy \Big/ \iint \theta \; dxdy \tag{13c}$$

Above variances were then assembled to form the covariance matrix

$$\Sigma = \begin{bmatrix} \sigma_{xx} & \sigma_{xy} \\ \sigma_{yx} & \sigma_{yy} \end{bmatrix} \tag{14}$$

The eigenvalues of the covariance matrix Σ, denoted as σ_a^2 and σ_b^2, represent the fractional variance experienced along the major and the minor axis of a hypothetical Gaussian cloud that could be fitted to the deformed tracer patch. The hypothetical Gaussian cloud then has an effective variance $\sigma^2 = 2\sigma_a\sigma_b$. Figure 7e shows the time evolution of ensemble averaged σ^2 for the QG and the SW flows. As expected, much higher values of σ^2 are observed for the SW flow when compared with the QG flow. Since the tracer blobs are initially small in size, the rapid increase of σ^2 on early timescales in the SW case compared to the QG case is an indication of the enhanced stirring at small scales in the SW case.

To estimate an effective diffusivity experienced by the tracer patch, we fit a straight line to the the variance data using the method of least squares to obtain the relationship $\sigma^2 = 4\mathcal{K}t + C$, so that differentiating with respect to time gives us the diffusivity: $\mathcal{K} = (1/4)d\sigma^2/dt$. We applied the linear fit to the time interval $t = 150$–200, sufficiently away from initial transients. Using this procedure, we computed $\mathcal{K}$ for the QG and SW cases and found that $(\mathcal{K}_{SW}/\mathcal{K}_{QG})_{t=150-200} = 4.42$. On longer timescales we observed that SW flow's diffusivity further increased; notice that a tendency for further increase in σ^2 can be gleaned from the final stages of the red curve in Figure 7e. However, as mentioned earlier, tracer patches were seen to be severely ruptured and dissipated at grid scale on such long timescales, due to which we kept our freely evolving experiments' duration to $\Delta t = 200$.

Overall, our freely evolving locally initialized tracer experiments compliment the qualitative conclusions from Section 3 based on forced dissipative experiments. SW flow stirs and mixes tracer patches much more effectively than the QG flow, resulting in about to five times higher diffusivity and lower mixing time.

5. Summary and Discussion

Over the past one decade a wide range of datasets, including in situ oceanic observations and high resolution global scale ocean model outputs, indicate increased levels of gravity wave energy on transitioning from mesoscales to submesoscales in the world's oceans. Investigations, using three-dimensional Boussinesq equations and reduced two-dimensional models, reveal breaking up of coherent vortices and formation of energetic small-scale dynamics in wave-dominated turbulent regimes (TY, Thomas & Arun, 2020; Thomas & Daniel, 2020, 2021). Although the specific energy transfer details depend on the kind of wave field, turbulent dynamics of wave-dominated regimes are in general significantly different from quasi-geostrophic regimes, the latter consisting of well-defined large-scale coherent vortices. The barotropic flow of the two-vertical-mode model explored by TY is an idealized flow that undergoes a transition in its turbulent features in high wave energy regimes. In the

absence of waves, the barotropic energy accumulates in large coherent vortices, as expected in the quasi-geostrophic (QG) regime. On the other hand, wave-dominated SW regime with $E_T/E_W \sim Ro^2$ is characterized by generation of energetic small-scale structures and breaking up of coherent vortices. The barotropic flow therefore is an idealized flow whose dynamic features transitions in moving from QG to SW regime. To explore the changes in tracer dispersion characteristics in the two different regimes using the simplest possible set up, in this work we treated the barotropic flow as a "prototype flow" that captures the qualitative dynamic features of QG and SW regimes and analyzed tracer dispersion in the two regimes.

For comparing flows of similar strengths, we generated barotropic flows with $E_T \sim Ro^2$ in both QG and SW regimes. While no waves were initialized in the QG case, we initialized waves with $E_W \sim 1$ in the SW case. Once the barotropic flows were fully developed, we advected passive tracer fields by the flows. We first examined turbulent dynamics of an equilibrated passive tracer field that was maintained by external forcing at large scales and dissipated at small scales. Although forced at large scales, stirring by the flow generates fine scale features in the tracer field, resulting in tracer variance cascading to small scales and getting dissipated. In the QG regime we found that the most efficient stirring of the tracer field was in high straining regions between coherent vortices. In contrast, the SW flow was characterized by enhanced stirring all over the domain with fine scales being continuously generated in the tracer field. Our examination of tracer fluxes pointed out that the SW flow lead to higher tracer variance flux over a larger fraction of physical domain when compared to the QG flow, resulting in increased stirring and mixing features of the SW flow when compared to the QG flow. On examining tracer norms, we found that although stirring of the tracers were more or less comparable at large scales, energetic small scales in the flow resulted in SW flow being more efficient than QG flow in stirring the tracers. Concomitantly, the timescale of mixing was seen to be lower for the SW flow when compared with the QG flow.

We followed up the forced-dissipative experiments with freely evolving tracer experiments where tracer fields were initialized locally as Gaussian blobs. The freely evolving tracer experiments were inspired by routine oceanographic cruises that measure turbulent diffusivity of oceanic flows by releasing dye tracers in the ocean and then monitoring their spreading with time. Complementary to our forced tracer experiments, the freely evolving experiments also revealed more efficient stirring by the SW flow with a smaller mixing timescale when compared to the QG flow. Tracer variance at early times was seen to increase much more rapidly in the SW case relative to the QG case, indicating enhanced stirring of tracers at smaller scales. On examining the turbulent diffusivity of the flows by quantifying the stirring of the tracer blobs, we found that the SW flow had higher diffusivity overall, with SW flow's diffusivity being about to five times higher value than that of the QG flow's.

The findings described above point out that wave-dominated flows, rich in energetic small-scale structures formed by breaking up of coherent vortices due to wave-balance interactions, can enhance tracer dispersion, increase the turbulent diffusivity, and decrease mixing timescales of the flow. Notably, waves modify the flow, that stirs the tracer field, thereby indirectly influencing tracer dispersion. Multiple past studies have tried to examine the role played by waves in oceanic dispersion problems by time filtering and removing waves from the data, and then comparing the dispersion by the full data and time-filtered "wave-free" data (this procedure for example is implemented in the recent work by Rossby et al., 2021). Such a procedure often leads to the conclusion that fast waves simply fluctuates around and does not cause any effective dispersion. In regimes where waves are strong, such as the SW regime we examined, the wave field can significantly modify the mean flow (i.e., the time-averaged flow that remains after filtering fast fluctuations). Gravity waves modify the flow, leading to the generation of energetic small-scale mean flow structures, which in turn enhances tracer dispersion. The indirect role that waves play in enhancing tracer dispersion, summarized in schematics shown in Figure 8, is the central take home message of this study.

Our results also corroborates with those studies that have explored dispersion in the presence of internal tides. Recall that SW regime is expected to apply to oceanic regions where baroclinic tides are energetic. In this direction, observational work of Meyerjurgens et al. (2020) using surface drifters and realistic coastal region simulations analyzed by Suanda et al. (2018) indicate that baroclinic tides can increase dispersive characteristics of the flow. Specifically, Suanda et al. (2018) finds three to four times higher dispersion in regions with baroclinic tides, when compared with scenarios that lack baroclinic tides. Once again, although direct comparisons between these studies and our idealized set up is challenging, the numbers reported in these studies are of comparable magnitude to the changes we found in our study, such as the tracer diffusivity shown in Figure 7e being four to five times higher in the SW regime when compared to the QG regime. We therefore speculate that the mechanism sketched

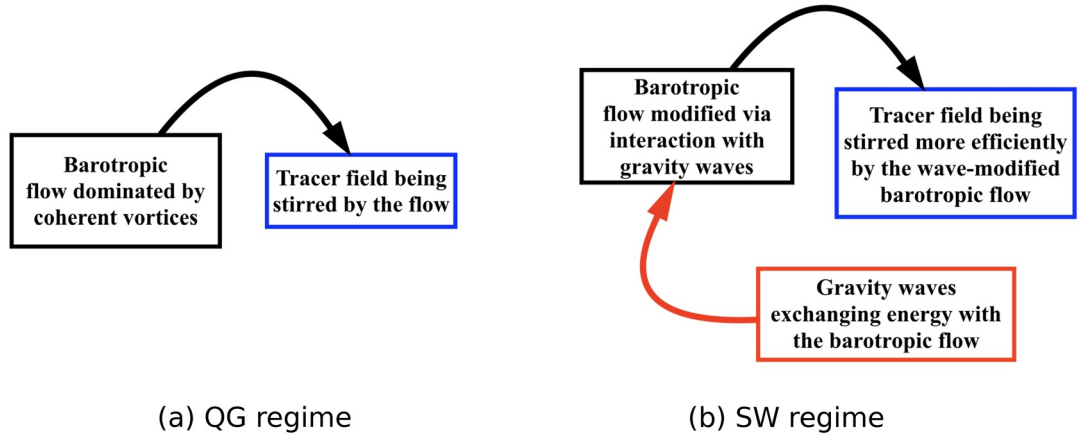

Figure 8. Schematics showing the gist of the tracer dispersion phenomenology in QG (left panel) and SW regimes (right panel). The black box represents the barotropic flow, the red box represents gravity waves, and the blue box represents the tracer field. In the QG regime, the barotropic flow is dominated by large-scale coherent vortices and straining regions between vortices are active sites of tracer stirring. In contrast, gravity waves exchange energy with the barotropic flow and generate energetic small-scale features in the flow. This modified barotropic flow stirs tracers much more efficiently when compared to the case in the QG regime. Gravity waves therefore play an indirect role, by modifying the barotropic flow, which in turn advects tracers. The indirect role played by gravity waves in enhancing tracer dispersion is the key finding of this study.

in Figure 8, of waves indirectly modifying the flow which in turn enhances tracer dispersion, might be operating in oceanic regions where baroclinic tides are strong.

We conclude by reminding the reader that the present work that considered tracer stirring by barotropic flow is a severe idealization of a complex three-dimensional oceanographic process. As mentioned earlier, interior parts of the ocean are often seen to have much steeper tracer spectra than that predicted based on quasi-geostrophic turbulence phenomenology (see datasets and discussions in Callies & Ferrari, 2013; Cole & Rudnick, 2012; Cole et al., 2010; Ferrari & Rudnick, 2000; Klymak et al., 2015; Kunze et al., 2015). Given the myriads of processes that operate at submesoscales, it is highly nontrivial to separate out the distinct mechanisms that contribute toward steep tracer spectra in above mentioned oceanic regions. Furthermore, as pointed out by Galperin and Sukoriansky (2020) and Galperin et al. (2021), spectral slope alone is insufficient to uniquely identify the dynamics. Amplitudes of the flow variables, level of anisotropy, and the fluxes of the flow variables are inevitable to associate features that are seen in oceanic observations with corresponding physical processes. By choosing to advect tracer fields in the QG and SW regimes by the barotropic flow alone, multiple realistic ingredients – such as vertical shear, baroclinic submesoscale vortices, and small-scale wave breaking events – that contributes toward tracer dispersion in the real ocean was ignored. Despite these shortcomings, the higher tracer variance flux (Figure 5) and steeper tracer variance spectra (Figure 6b) in the SW regime compared to the QG regime seen in our set up suggests that wave enhanced tracer dispersion might play an important role in wave dominant oceanic regions discussed earlier. Of course, quantifying tracer dispersion in QG and SW regimes by incorporating the missing ingredients of this study requires dedicated fully three-dimensional explorations using the non-hydrostatic Boussinesq equations. We hope to undertake such three-dimensional investigations to complement the present work in the near-future.

Appendix A: Tracer Dispersion by Compressible Flows

In this work we treated the barotropic flow as an idealized prototype flow that captures the essence of the flow transition between QG and SW regimes and analyzed tracer dispersion using the barotropic flow alone. Referring to the full set of Equations 1a–1c, one may anticipate advecting tracer fields with both barotropic and baroclinic velocity fields, instead of the barotropic field alone. However, quantifying results from such a tracer dispersion experiment becomes challenging, since the baroclinic velocity field is divergent, that is, $\nabla \cdot \boldsymbol{v}_C \neq 0$. To see the difficulty explicitly, recall that if the advecting velocity field is divergence free, in the absence of forcing and dissipative effects, tracer variance integrated over the domain is conserved in time. This can be seen by setting

$f_\theta = \alpha = 0$ in Equation 3 and multiplying the resulting equation by θ and integrating over the domain, which leads to $d<\theta^2>/dt = 0$, where $< >$ indicates integration over the whole domain. The manipulations leading to the result requires the advecting velocity field to be divergence free, implying that tracer variance will not be conserved if tracer field is advected by a divergent velocity field. A similar issue arises in shallow water equations, where tracer variance is not conserved in the inviscid limit; rather it is the product of height and tracer variance that is conserved. It is noteworthy that none of these ambiguities appear in the hydrostatic Boussinesq equations, from which the reduced model (Equation 1) is derived, since the three-dimensional velocity field in the Boussinesq equations is divergence free. For more detailed discussions on features and techniques to quantify tracer dispersion by divergent velocity fields, we refer the reader to Thiffeault (2021).

As part of this work we did explore advecting tracer fields with both barotropic and baroclinic velocity fields. The qualitative results described earlier, specifically smaller scale baroclinic features in the flow advecting tracer fields more efficiently, was observed in SW regime. This is not surprising, since the baroclinic flow in the SW regime generates small-scale vortical features, just like the barotropic flow (see e.g., Figure 4b and related discussion in TY). Despite the similarity in qualitative features, the corresponding forms of tracer variance equations such as Equation 5 in the presence of non-divergent baroclinic velocity field is much more cumbersome. To examine the tracer dispersion characteristics in two different regimes using the simplest setting possible, we eliminated the extra complexities introduced by involving the full divergent baroclinic mode, and advected the tracer fields with the barotropic flow alone in the present work.

Data Availability Statement

Datasets and codes corresponding to the results presented in this manuscript are available in the repository: https://zenodo.org/record/5874936.

Acknowledgments
Stimulating discussions on general features of passive tracer dispersion with Jean-Luc Thiffeault inspired the usage of mixed norm Equation 6 for analyzing stirring efficiencies of tracers at different scales. Anonymous reviewers are thanked for comments and suggestions that improved the presentation of results in this paper.

References

Alvelius, K. (1999). Random forcing of three-dimensional homogeneous turbulence. *Physics of Fluids*, *11*, 1880–1889. https://doi.org/10.1063/1.870050

Benilov, E. S., & Wolanski, E. (1992). A note on the diffusion in fluids with wave-induced random motion: Applications to the barotropic Rossby waves. *Physics of Fluids A*, *4*, 58–62. https://doi.org/10.1063/1.858500

Bühler, O., Callies, J., & Ferrari, R. (2014). Wave-vortex decomposition of one-dimensional ship-track data. *Journal of Fluid Mechanics*, *756*, 1007–1026. https://doi.org/10.1017/jfm.2014.488

Buhler, O., & Holmes-Cerfon, M. (2009). Particle dispersion by random waves in rotating shallow water. *Journal of Fluid Mechanics*, *638*, 5–26. https://doi.org/10.1017/s0022112009991091

Callies, J., & Ferrari, R. (2013). Interpreting energy and tracer spectra of upper-ocean turbulence in the submesoscale range (1–200 km). *Journal of Physical Oceanography*, *43*, 2456–2474. https://doi.org/10.1175/jpo-d-13-063.1

Cole, S., & Rudnick, D. (2012). The spatial distribution and annual cycle of upper ocean thermohaline structure. *Journal of Geophysical Research*, *117*, C02027. https://doi.org/10.1029/2011jc007033

Cole, S., Rudnick, D., & Colosi, J. (2010). Seasonal evolution of upper-ocean horizontal structure and the remnant mixed layer. *Journal of Geophysical Research*, *115*, C04012. https://doi.org/10.1029/2009jc005654

Csanady, G. T. (1980). *Turbulent diffusion in the environment*. D. Reidel Publishing.

Ferrari, R., & Rudnick, D. (2000). Thermohaline variability in the upper ocean. *Journal of Geophysical Research*, *105*, 16857–16884. https://doi.org/10.1029/2000jc900057

Fischer, H. B., List, E. J., Koh, R. C. Y., Imberger, J., & Brooks, N. H. (1979). *Mixing in inland and coastal waters*. Academic.

Galperin, B., & Sukoriansky, S. (2020). Quasinormal scale elimination theory of the anisotropic energy spectra of atmospheric and oceanic turbulence. *Physical Review Fluids*, *5*, 063803. https://doi.org/10.1103/physrevfluids.5.063803

Galperin, B., Sukoriansky, S., & Qiu, B. (2021). Seasonal oceanic variability on meso- and submesoscales: A turbulence perspective. *Ocean Dynamics*, *71*, 475–489. https://doi.org/10.1007/s10236-021-01444-1

Holmes-Cerfon, M., Buhler, O., & Ferrari, R. (2011). Particle dispersion by random waves in the rotating Boussinesq system. *Journal of Fluid Mechanics*, *670*, 150–175. https://doi.org/10.1017/s0022112010005240

Klein, P., Treguier, A. M., & Hua, B. L. (1998). Three-dimensional stirring of thermohaline fronts. *Journal of Marine Research*, *56*, 589–612. https://doi.org/10.1357/002224098765213595

Klymak, J. M., Crawford, W., Alford, M. H., MacKinnon, J. A., & Pinkel, R. (2015). Along-isopycnal variability of spice in the north pacific. *Journal of Geophysical Research: Oceans*, *120*, 2287–2307. https://doi.org/10.1002/2013jc009421

Kunze, E., Klymak, J. M., Lien, R. C., Ferrari, R., Lee, M. A., Sundermeyer, C. M., & Goodman, L. (2015). Submesoscale water-mass spectra in the Sargasso Sea. *Journal of Physical Oceanography*, *45*, 1325–1338. https://doi.org/10.1175/jpo-d-14-0108.1

Ledwell, J., Watson, A., & Law, C. (1993). Evidence for slow mixing across the pycnocline from an open-ocean tracer-release experiments. *Nature*, *364*, 701–703. https://doi.org/10.1038/364701a0

Lelong, M.-P., & Sundermeyer, M. A. (2005). Geostrophic adjustment of an isolated diapycnal mixing event and its implications for small-scale lateral dispersion. *Journal of Physical Oceanography*, *35*, 2352–2367. https://doi.org/10.1175/jpo2835.1

Lien, R.-C., & Sanford, T. B. (2019). Small-scale potential vorticity in the upper ocean thermocline. *Journal of Physical Oceanography*, *49*, 1845–1872. https://doi.org/10.1175/jpo-d-18-0052.1

Lindzen, R. S. (1981). Turbulence and stress owing to gravity wave and tidal breakdown. *Journal of Geophysical Research*, *86*, 9707–9714. https://doi.org/10.1029/jc086ic10p09707

Majda, A. J. M., & Kramer, P. R. (1999). Simplified models for turbulent diffusion: Theory, numerical modelling, and physical phenomena. *Physics Reports*, *314*, 237–574. https://doi.org/10.1016/s0370-1573(98)00083-0

McWilliams, J. C. (2016). Submesoscale currents in the ocean. *Proceedings of the Royal Society*, *A472*, 20160177. https://doi.org/10.1098/rspa.2016.0117

Meyerjurgens, J., Ricker, M., Schakau, V., Badewien, T. H., & Stanev, E. V. (2020). Relative dispersion of surface drifters in the North Sea: The effect of tides on mesoscale diffusivity. *Journal of Geophysical Research: Oceans*, *124*, e2019JC015925. https://doi.org/10.1029/2019jc015925

Peeters, F., Wilest, A., Piepke, G., & Imboden, D. M. (1996). Horizontal mixing in lakes. *Journal of Geophysical Research*, *101*, 18361–18375. https://doi.org/10.1029/96jc01145

Polzin, K. L., & Ferrari, R. (2004). Isopycnal dispersion in nature. *Journal of Physical Oceanography*, *34*, 247–257. https://doi.org/10.1175/1520-0485(2004)034<0247:idin>2.0.co;2

Pope, S. B. (2000). *Turbulent flows*. Cambridge University Press.

Qi, D., & Majda, A. J. (2018). Predicting extreme events for passive scalar turbulence in two-layer baroclinic flows through reduced-order stochastic models. *Communication in Mathematical Sciences*, *16*, 17–51. https://doi.org/10.4310/cms.2018.v16.n1.a2

Qiu, B., Chen, S., Klein, P., Wang, J., Torres, H., Fu, L., & Menemenlis, D. (2018). Seasonality in transition scale from balanced to unbalanced motions in the world ocean. *Journal of Physical Oceanography*, *48*, 591–605. https://doi.org/10.1175/jpo-d-17-0169.1

Qiu, B., Nakano, T., Chen, S., & Klein, P. (2017). Submesoscale transition from geostrophic flows to internal waves in the northwestern pacific upper ocean. *Nature Communications*, *8*, 14055. https://doi.org/10.1038/ncomms14055

Randel, W. J., & Garcia, R. R. (1994). Application of a planetary wave breaking parameterization to stratospheric circulation statistics. *Journal of Physical Oceanography*, *51*, 1157–1168. https://doi.org/10.1175/1520-0469(1994)051<1157:aoapwb>2.0.co;2

Richardson, P. L. (2008). On the history of meridional overturning circulation schematic diagrams. *Progress in Oceanography*, *76*, 466–486. https://doi.org/10.1016/j.pocean.2008.01.005

Richman, J. G., Arbic, B. K., Shriver, J. F., Metzger, E. J., & Wallcraft, A. J. (2012). Inferring dynamics from the wavenumber spectra of an eddying global ocean model with embedded tides. *Journal of Geophysical Research*, *117*, C12012. https://doi.org/10.1029/2012jc008364

Rocha, C. B., Chereskin, T. K., Gille, S. T., & Menemenlis, D. (2016). Mesoscale to submesoscale wavenumber spectra in drake passage. *Journal of Physical Oceanography*, *46*, 601–620. https://doi.org/10.1175/jpo-d-15-0087.1

Rossby, T., Omand, M., Palter, J., & Hebert, D. (2021). On rates of isopycnal dispersion at the submesoscale. *Geophysical Research Letters*, *48*, e2021GL093526. https://doi.org/10.1029/2021gl093526

Sanderson, B. G., & Okubo, A. (1988). Diffusion by internal waves. *Journal of Geophysical Research*, *93*, 3570–3582. https://doi.org/10.1029/jc093ic04p03570

Savage, A., Arbic, B. K., Alford, M. H., Ansong, J. K., Farrar, J. T., Menemenlis, D., et al. (2017). Spectral decomposition of internal gravity wave sea surface height in global models. *Journal of Geophysical Research: Oceans*, *122*, 7803–7821. https://doi.org/10.1002/2017jc013009

Scott, R. K. (2006). Local and nonlocal advection of a passive scalar. *Physics of Fluids*, *56*, 122–125. https://doi.org/10.1063/1.2375020

Shcherbina, A. Y., Kunze, E., D'Asaro, E., Badin, G., Birch, D., Brunner-Suzuki, A.-M. E. G., et al. (2015). The LatMix summer campaign: Submesoscale stirring in the upper ocean. *Bulletin of the American Meteorological Society*, *96*, 1257–1279. https://doi.org/10.1175/bams-d-14-00015.1

Shuckburgh, E. F., & Haynes, P. H. (2003). Diagnosing tracer transport and mixing using a tracer-based coordinate system. *Physics of Fluids*, *15*, 3342–3357. https://doi.org/10.1063/1.1610471

Smith, K. S., & Ferrari, R. (2009). The production and dissipation of compensated thermohaline variance by mesoscale stirring. *Journal of Physical Oceanography*, *39*, 2477–2501. https://doi.org/10.1175/2009jpo4103.1

Spiro Jaeger, G., MacKinnon, J. A., Lucas, A. J., Shroyer, E., Nash, J., Tandon, A., et al. (2020). How spice is stirred in the Bay of Bengal. *Journal of Physical Oceanography*, *50*, 2669–2688. https://doi.org/10.1175/jpo-d-19-0077.1

Suanda, S. H., Feddersen, F., Spydell, M. S., & Kumar, N. (2018). The effect of barotropic and baroclinic tides on three-dimensional coastal dispersion. *Geophysical Research Letters*, *45*, 11235–11246. https://doi.org/10.1029/2018gl079884

Sukoriansky, S., Dikovskaya, N., & Galperin, B. (2009). Transport of momentum and scalar in turbulent flows with anisotropic dispersive waves. *Geophysical Research Letters*, *36*, L14609. https://doi.org/10.1029/2009gl038632

Sundermeyer, M., & Ledwell, J. (2001). Lateral dispersion over the continental shelf: Analysis of dye release experiments. *Journal of Geophysical Research*, *106*, 9603–9621. https://doi.org/10.1029/2000jc900138

Sundermeyer, M. A., Birch, D. A., Ledwell, J. R., Levine, M. D., Pierce, S. D., & Cervantes, B. T. K. (2019). Dispersion in the open ocean seasonal pycnocline at scales of 1-10 km and 1-6 days. *Journal of Physical Oceanography*, *49*, 415–437.

Sundermeyer, M. A., & Lelong, M.-P. (2005). Numerical simulations of lateral dispersion by the relaxation of diapycnal mixing events. *Journal of Physical Oceanography*, *35*, 2368–2386. https://doi.org/10.1175/jpo2834.1

Taylor, G. I. (1922). Diffusion by continuous movements. *Proceedings of the London Mathematical Society*, *2*, 196–212. https://doi.org/10.1112/plms/s2-20.1.196

Tchilibou, M., Gourdeau, L., Morrow, R., Serazin, G., Djath, B., & Lyard, F. (2018). Spectral signatures of the tropical pacific dynamics from model and altimetry: A focus on the meso/submesoscale range. *Ocean Science*, *14*, 1283–1301. https://doi.org/10.5194/os-14-1283-2018

Thiffeault, J.-L. (2012). Using multiscale norms to quantify mixing and transport. *Nonlinearity*, *25*, R1–R44. https://doi.org/10.1088/0951-7715/25/2/r1

Thiffeault, J.-L. (2021). Nonuniform mixing. *Physical Review Fluids*, *6*, 090501. https://doi.org/10.1103/physrevfluids.6.090501

Thomas, J., & Arun, S. (2020). Near-inertial waves and geostrophic turbulence. *Physical Review Fluids*, *5*, 014801. https://doi.org/10.1103/physrevfluids.5.014801

Thomas, J., & Daniel, D. (2020). Turbulent exchanges between near-inertial waves and balanced flows. *Journal of Fluid Mechanics*, *902*, A7. https://doi.org/10.1017/jfm.2020.510

Thomas, J., & Daniel, D. (2021). Forward flux and enhanced dissipation of geostrophic balanced energy. *Journal of Fluid Mechanics*, *911*, A60. https://doi.org/10.1017/jfm.2020.1026

Thomas, J., & Yamada, R. (2019). Geophysical turbulence dominated by inertia-gravity waves. *Journal of Fluid Mechanics*, *875*, 71–100. https://doi.org/10.1017/jfm.2019.465

Torres, H. S., Klein, P., Menemenlis, D., Qiu, B., Su, Z., Wang, J., et al. (2018). Partitioning ocean motions into balanced motions and internal gravity waves: A modeling study in anticipation of future space missions. *Journal of Geophysical Research: Oceans*, *123*, 8084–8105. https://doi.org/10.1029/2018jc014438

Warren, B. A., & Wunsch, C. (1981). *Evolution of Physical Oceanography: Scientific Surveys in Honor of Henry Stommel* (Vol. 664, pp. 6–41). The MIT Press.

Wunsch, C., & Ferrari, R. (2018). 100 years of the ocean general circulation. Chapter 7. *Meteorological Monographs*, *59*, 7.1–7.32. https://doi.org/10.1175/amsmonographs-d-18-0002.1